

# Aqueous Rechargeable Manganese/Iodine Battery

Vaiyapuri Soundharajan<sup>+[a]</sup> Duong Tung Pham<sup>+[b]</sup> Junji Piao,<sup>[a]</sup> Subramanian Nithiananth,<sup>[c]</sup> Jung Ho Kim,<sup>\*[d]</sup> and Jaekook Kim<sup>\*[a, e]</sup>

Carbon neutralization has promoted the identification of new types of energy storage devices. Aqueous iodine batteries (AlBs) with reversible iodine redox activity are considered a viable candidate for stationary energy storage units and thus have recently drawn extensive research interest. Herein, we introduce an aqueous manganese iodine battery (AMIB), utilizing sodium iodide (NaI) as a redox-active additive in the  $\text{Mn}(\text{ClO}_4)_2$  (NMC) electrolyte, activated carbon (AC) as a redox host and Mn ions as the charge carrier. Taking advantage of enhanced kinetics facilitated by  $\text{I}_2/2\text{I}^-$  redox activity, our suggested AMIBs can be electrochemically charged/discharged with only a 6 % loss in

capacity after 2,000 cycles at a low current density of  $0.3 \text{ A g}^{-1}$  in an AC||AC coin cell configuration. Moreover, the AC||Zn–Mn hybrid full-cell configuration is also established with AC and a Zn–Mn anode involving the NMC electrolyte, which retains a high energy of  $185 \text{ Wh kg}^{-1}$  at a specific power of  $2,600 \text{ W kg}^{-1}$ . Overall, the AMIBs in this study preferred  $\text{I}_2/\text{I}^-$  conversion chemistry, yielding stable cycle stability, rate performance, and low capacity loss per cycle when compared to Manganese Ion Batteries (MIBs) which are based on  $\text{Mn}^{2+}$  intercalation chemistry.

## 1. Introduction

The modern electronic world mainly depends on two distinct battery systems: lead-acid batteries (Pb-acid) and lithium-ion batteries (LIBs).<sup>[1,2]</sup> Specifically, LIBs are not only a promising power source for portable electronics, but they are also crucial for e-mobility vehicles.<sup>[3–5]</sup> Nevertheless, given the characteristic shortcomings associated with Pb-acid batteries (toxicity) and LIBs (safety challenges and high price), a dependable energy storage system is needed to store electricity safely and economically.<sup>[1,6–8]</sup> In this regard, diverse energy storage hubs involving aqueous electrolytes comprising zinc-ion batteries

(ZIBs), aluminum-ion batteries (AlIBs), manganese-ion batteries (MIBs), and nickel-ion batteries (NIBs) have recently been introduced.<sup>[9–15]</sup> However, these ion batteries are primarily driven by intercalation chemistry, where the intercalation host suffers from structural failures associated with the strong electrostatic interaction of multivalent ions.<sup>[16,17]</sup>

The eco-friendly nature of iodine (I) combined with its reversible high-capacity ( $\sim 210 \text{ mAh g}^{-1}$ ) conversion mechanism ( $\text{I}_2/2\text{I}^-$ ) has paved the way for the development of aqueous iodine batteries (AlBs).<sup>[18,19]</sup> On the cathode side, porous carbon is suggested as a host to confine iodine; depending on the surface area of the carbon host and interfacial features, the capacity, rate output, and cycling stability vary significantly.<sup>[20–22]</sup> However, diverse metals, including Zn, Fe, and Al are used for the anode due to the high-capacity and low-cost formulation of Zn–I<sub>2</sub>, Fe–I<sub>2</sub>, and Al–I<sub>2</sub> batteries.<sup>[23–25]</sup> In this regard, the recent arrival of an MIB utilizing a low-cost and high-capacity metallic manganese anode inspired us to investigate the potential of aqueous Mn–I<sub>2</sub> batteries (AMIBs).<sup>[26]</sup> The Zn/Zn<sup>2+</sup> oxidation-reduction potential of ( $-0.763 \text{ V}$ ) vs the standard hydrogen electrode (SHE) is higher than that of Mn/Mn<sup>2+</sup> ( $-1.17 \text{ V}$ ). This means that the working voltage of Mn–I<sub>2</sub> could be higher than that of the Zn–I<sub>2</sub> battery if conventional Mn metal is used as an anode.<sup>[27–30]</sup> Bi et al. established the feasibilities of various metal-iodine batteries with six-electron reactions involving I<sub>2</sub>@AC cathode and electrolytes with the coexistence of redox-ion carriers and halide ions.<sup>[31]</sup> They also revealed the possible formation of a Mn||I<sub>2</sub> battery using I<sub>2</sub>@AC as the cathode and Mn powder as the anode, with 1 M MnSO<sub>4</sub>/0.5 M MnCl<sub>2</sub> as the electrolyte. However, the electrochemical properties and cycling stability have not been thoroughly explored.

Thus for the construction of conventional aqueous-iodine batteries, porous carbon is impregnated with I<sub>2</sub> using a metal-diffusion or solution-adsorption process and used as a positive electrode.<sup>[14,32]</sup> However, using solid-bulk iodine as a cathode presents difficulties due to its insulating nature and the

[a] V. Soundharajan,<sup>+</sup> J. Piao, J. Kim

Department of Materials Science and Engineering, Chonnam National University, 77 Yongbong-ro, Bukgu, Gwangju 61186, Republic of Korea  
Fax: +82-62-530-1669

Tel: +82-62-530-17  
E-mail: jaekook@chonnam.ac.kr

[b] D. T. Pham<sup>+</sup>

School of Engineering Physics, Hanoi University of Science and Technology, No 1 Dai Co Viet Street, 100000, Hanoi, Viet Nam

[c] S. Nithiananth

Graduate School of Science and Technology, Shizuoka University, 3-5-1 Johoku, Naka-ku, Hamamatsu, Shizuoka, 432-8011, Japan

[d] J. H. Kim

Institute for Superconducting and Electronic Materials (ISEM), Australian Institute of Innovative Materials (AIIM), University of Wollongong, North Wollongong, New South Wales, 2500, Australia  
E-mail: jhk@uow.edu.au

[e] J. Kim

Research Center for Artificial Intelligence Assisted Ionics Based Materials Development Platform, Chonnam National University, Gwangju, 61186, Republic of Korea

[+] These two authors contributed equally. The manuscript was written through the contributions of all authors. All authors have approved the final version of the manuscript.

 Supporting information for this article is available on the WWW under <https://doi.org/10.1002/batt.202400131>

generation of soluble solid co-products during the cycling of the cells. Notably, the  $\text{I}^-$  species in the electrolyte interacts with the solid bulk iodine to form soluble triiodide ( $\text{I}_3^-$ ), which then migrates to the anode side and oxidizes the metal anode, resulting in rapid self-discharge issues.<sup>[33]</sup> Electrochemical engineers have made design changes to overcome these problems, such as the use of cation exchange membranes or customised functional layers including MOF membranes, PEDOT: PSS nanopapers, silicon-based anti-corrosion films, and zeolite-based anti-corrosion films.<sup>[34–37]</sup> Iodine's low solvation energy in the aqueous electrolyte causes it to be strongly absorbed in the cathode surface, and researchers have identified that electrolyte composition is critical.<sup>[38]</sup> Specifically, the introduction of iodine redox additives into electrolytes enabled iodine-free positive electrodes to be used in designing high-energy redox-active energy storage devices.<sup>[39,40]</sup> The  $\text{I}_2$  can be electrochemically reversibly deposited onto the activated carbon (AC) electrodes from redox-active electrolytes like KI or  $\text{Zn}-\text{I}_2$ .<sup>[41,42]</sup> The redox-active electrolyte strategy could significantly reduce production costs since no specific care needs to be taken to load  $\text{I}_2$  onto positive electrodes.<sup>[43–45]</sup>

Moreover, the volumetric and gravimetric energy densities could be improved significantly when AC alone used as cathode.<sup>[46,47]</sup> This study aims to establish an aqueous manganese iodine battery (AMIB) using NaI as a redox-active electrolyte. The proposed design is motivated by the electrochemical deposition/dissolution of iodine from alkaline iodides.<sup>[33,48]</sup> In specific, for the construction of AMIBs, we utilized 0.1 M NaI as a redox additive to the 1 M  $\text{Mn}(\text{ClO}_4)_2$  (NMC) as an electrolyte. More importantly, we used commercial AC with a sizable surface area ( $1329 \text{ m}^2 \text{ g}^{-1}$ ) as a positive electrode and the related electrochemical  $\text{I}_2/2\text{I}^-$  redox mechanism is illustrated in Figure 1. In specific, the electrolyte clouds (NMC) are loaded onto the AC surface where it serves as the  $\text{I}_2$  host. During the charging process,  $\text{I}^-$  ions in the electrolyte are converted into  $\text{I}_2$  particles through electrochemical iodization. This process is

reversible, and the corresponding electrochemical process leads to the formulation of AMIBs. Thus benefiting from the reversible  $\text{I}_2/2\text{I}^-$  redox features, the fabricated AMIBs in the  $\text{AC}||\text{AC}$  coin cell configuration sustained a stable cycling life of close to 2000 cycles at  $0.3 \text{ A g}^{-1}$  with a low-capacity loss per cycle (0.06%), a high-rate output of  $121 \text{ mAh g}^{-1}$  at  $2.0 \text{ A g}^{-1}$ , and an extreme cycle life with 91% capacity retention over 10,000 cycles at  $2.0 \text{ A g}^{-1}$ .

## 2. Results and Discussion

First, AC was examined using XRD analysis (Figure S1a), and the amorphous broad peaks between  $20^\circ$  and  $30^\circ$  and  $43^\circ$  and  $50^\circ$  represented the (002) and (100) planes, respectively.<sup>[49]</sup> The AC showed a disordered graphitic form of amorphous carbon, which can be recognized by the presence of broad peaks.<sup>[47]</sup> Furthermore, TEM observation of the AC revealed that the sample exhibited a porous micro sheet-like structure (Figure S1b). The high-resolution TEM image also revealed the disordered carbon features of the AC (Figure S1c). In addition, the elemental features of the AC were differentiated by the XPS, which revealed the presence of C 1s and O 1s spectra (Figure S1d and S1e). The deconvoluted C 1s spectrum comprised three peaks at 284.5, 285.6, and 289.1 eV, assigned to  $\text{C}=\text{C}$  ( $\text{sp}^2$ -C hybridized),  $\text{C}-\text{O}$ , and  $\text{O}=\text{C}=\text{C}$  bonds, respectively.<sup>[50]</sup> Similarly, the deconvoluted O 1s spectra at 534, 532.7, and 531.9 eV were attributed to  $\text{O}=\text{C}$ ,  $\text{C}-\text{OH}$ , and  $\text{H}-\text{O}-\text{H}$ , respectively.<sup>[51]</sup> The nitrogen adsorption isotherm was measured to obtain detailed information on the specific surface area and pore size distribution of the AC. As an illustration, the IV isotherm exhibited a pronounced hysteresis loop, indicating the mesoporous structure of the AC (Figure S1f). Inset in Figure S1f, contains the pore size distribution plot. The BET surface area of the AC was revealed to be  $1329 \text{ m}^2 \text{ g}^{-1}$ , confirming its suitability as a capable reservoir for storing the redox-active ions. AC with

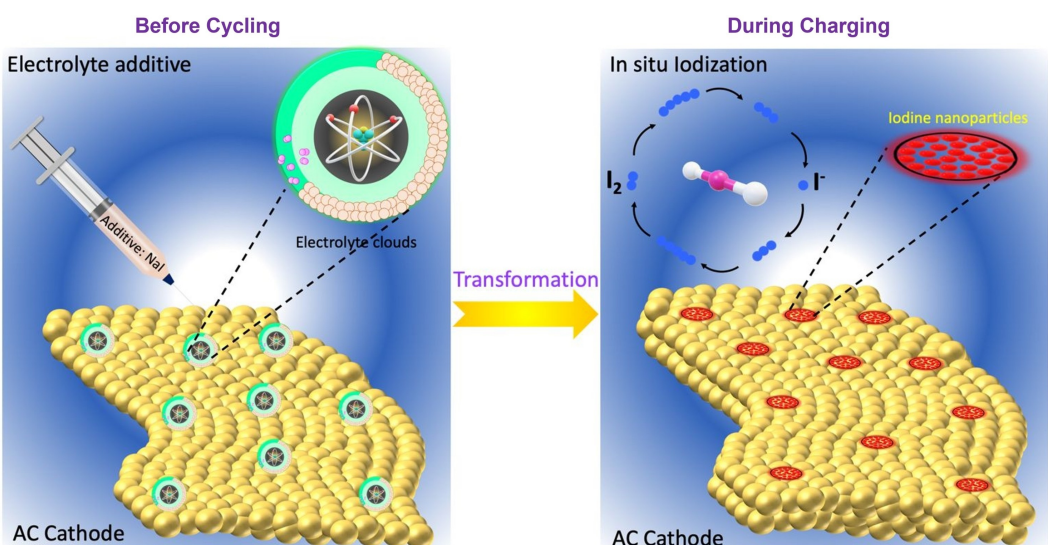


**Figure 1.** Schematic illustration of the electrochemical  $\text{I}_2/2\text{I}^-$  redox mechanism and the feasibility of AMIBs.

a high surface area has a large active site for facilitating electrochemical conversion reactions.<sup>[41,52]</sup>

To evaluate the electrochemical iodine storage properties of the AC, AC||AC coin cell was used in the presence of NMC electrolyte. The corresponding electrochemical results are shown in Figure 2. At 0.2 mVs<sup>-1</sup>, there was a single redox curve associated with the conversion of I<sub>2</sub>/2I<sup>-</sup> redox couples (Figure 2a).<sup>[53–55]</sup> This indicates that the AC promotes the electrochemical iodine deposition/dissolution process. Furthermore, the CV curves exhibited a clear overlapping in repeated cycling, indicating a highly reversible electrochemical iodine deposition/dissolution. The I<sub>2</sub>/2I<sup>-</sup> redox activity in the galvanostatic charge/discharge profile at 0.1 A g<sup>-1</sup> was consistent with the CV results (Figure 2b). Specifically, the AC cathode showed initial charge and discharge capacities of 118 and 180.5 mAh g<sup>-1</sup>, respectively. The voltage profile of the first charge cycle is slightly different from subsequent cycles and provides a lower specific capacity, which could be due to incomplete electrolyte impregnation in the AC cathode, resulting in partial iodization.

Thus, the lower charge capacity indicates that the 2I<sup>-</sup> was only partially iodized in the initial cycle, but became stabilized in the subsequent cycle, demonstrating a highly reversible iodine deposition/dissolution. In terms of rate performance, the AC cathode registered high discharge capacities of 180.5, 163, 152, 140.3, 131, and 121 mAh g<sup>-1</sup> at current densities of 0.1, 0.2, 0.5, 1.0, 1.5, and 2.0 A g<sup>-1</sup>, respectively (Figure 2c). The resultant voltage vs. capacity profiles are provided in Figure S2a, showing a nearly identical voltage curve with a small voltage polarization with increasing current rates. The cyclability profile at a low current rate of 0.3 A g<sup>-1</sup> is presented in Figure 2d. The cycling

output keeps a high-capacity retention of 94% after 2,000 cycles, maintaining a specific discharge capacity of 131.54 mAh g<sup>-1</sup>, where the initial discharge capacity is 138 mAh g<sup>-1</sup>. Cycling stability at low currents is essential for AIBs for long-term storage applications. Figure S2b presents the voltage vs. capacity curve for multiple cycles (2<sup>nd</sup>, 500<sup>th</sup>, 1000<sup>th</sup>, and 2000<sup>th</sup>), which retains the profile firmly, demonstrating AC's excellent reversible electrochemical iodine storage capability.

To evaluate the reaction kinetics of the iodine redox couples in the electrochemical capacity outputs, the CV analysis was performed with different scan rates of 0.2, 0.3, 0.4, 0.5, 0.6, 0.7, and 1.0 mVs<sup>-1</sup> (Figure 3a). The total current recorded from the CV output can be further divided into diffusion-induced charge capacity and capacitive charge capacity. As a result, the diffusion and capacitive outputs at a definite voltage can be determined using the following equation:<sup>[56–59]</sup>

$$i(v) = k_1 v + k_2 v^{1/2}, \quad (1)$$

where  $i(v)$  indicates the response current at a definite voltage (V),  $v$  denotes the scan rate,  $k_1 v$  represents the capacitive current, and  $k_2 v^{1/2}$  is associated with diffusion-induced kinetics. By plotting  $i(v)/v^{1/2}$  versus  $v^{1/2}$ , the constants  $k_1$  and  $k_2$  can be calculated from the slope ( $k_1$ ) and the intercept ( $k_2$ ). The calculated capacitive charge contribution of the AMIBs at a scan rate of 0.2 mVs<sup>-1</sup> is presented in Figure 3b. The ratios of the capacitive/diffusion charge contribution of the AMIBs system at different scan rates of 0.2, 0.3, 0.5, 0.7, and 1.0 mVs<sup>-1</sup> are found to be 54%, 58%, 68%, 73%, and 81%, respectively (Figure 3c).

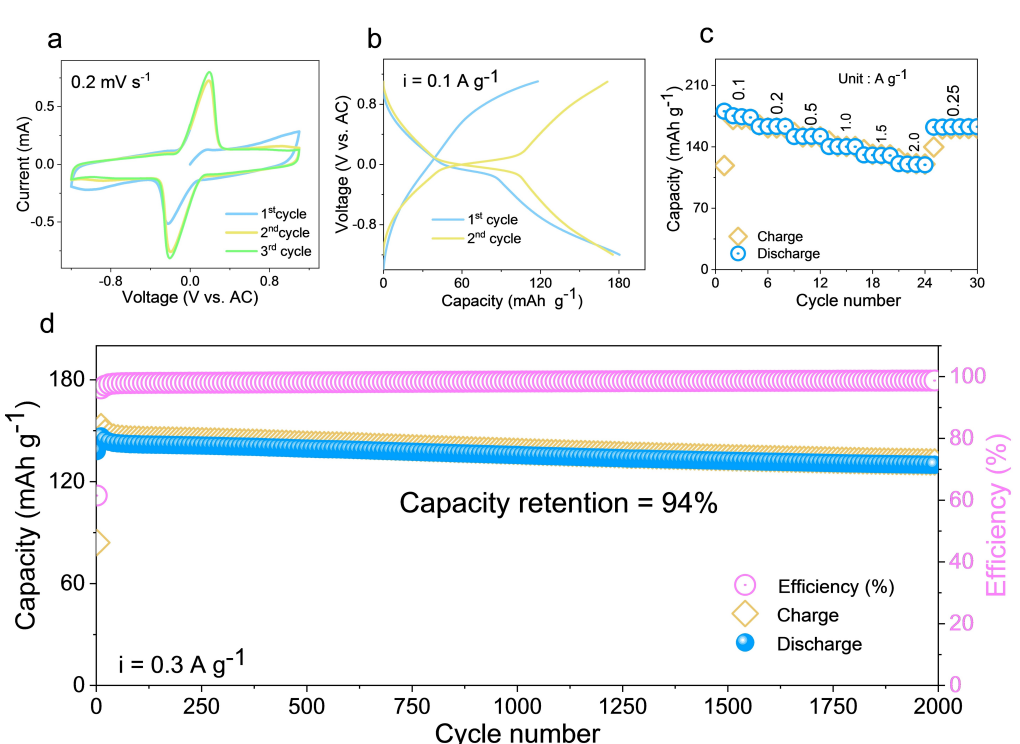


**Figure 2.** a) CV curves of AC cathode at 0.2 mVs<sup>-1</sup>, b) Voltage vs. capacity profiles of AC cathode at 0.1 A g<sup>-1</sup>, c) Rate capability profiles of AC cathode at different current rates, and d) cycle life of AC cathode at 0.3 A g<sup>-1</sup>.

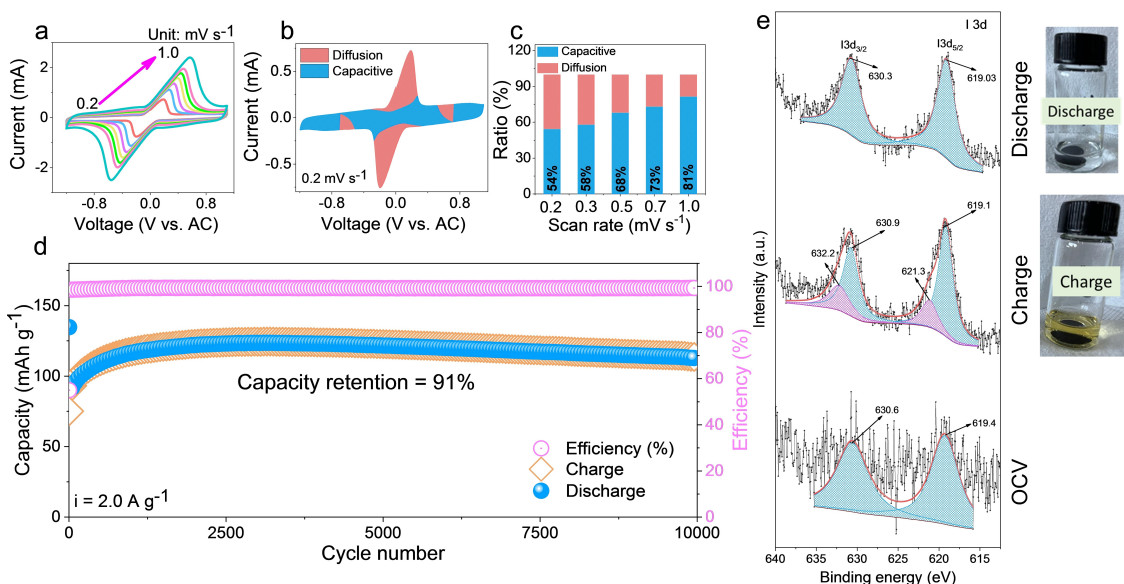


**Figure 3.** a) CV curves of AC cathode at various scan rates, b) capacitive and diffusion contributions calculated from CV scan at  $0.2 \text{ mV s}^{-1}$ , c) comparison of capacitive and diffusion contributions of AC cathode at different scan rates, d) cycle life of AC cathode at  $2.0 \text{ A g}^{-1}$ , and e) ex-situ XPS profile for I 3d feature in AC cathode at different electrochemical states. (Inset: Digital photograph of the AC cathode immersed in ethanol before/after cycling)

The instant iodine storage ability of the MIBs is further determined at a high current rate of  $2 \text{ A g}^{-1}$ , and the corresponding profile is shown in Figure 3d. It is evident that the AMIBs can consistently perform over 10,000 cycles, maintaining a capacity of  $113 \text{ mAh g}^{-1}$ . An examination of the cycling study revealed that after an initial registering capacity of  $84 \text{ mAh g}^{-1}$ , the cell showed an activation behavior and reached a maximum activated capacity of  $123.4 \text{ mAh g}^{-1}$  at the 2,920<sup>th</sup> cycle. Subsequently, the cycling stabilized, and the capacity was retained after 10,000 cycles at 91% of the maximum capacity, confirming the highly reversible nature of iodine redox activity at high current rates. Additionally, the voltage vs. capacity profiles also retained the shape of the curve for most of the cycling (Figure S2c), demonstrating that the electrochemical iodine deposition/dissolution is stable throughout the cycling process.

The iodine deposition/dissolution in the AMIBs was examined using the results of the ex-situ XPS studies in the different electrochemical states. Figure 3e displays the I 3d profile before and after the electrochemical process. Following the charging process, two strong peaks at 619.1 and 630.9 eV evolved on the surface of the AC cathode, corresponding to the (oxidized) I 3d features representing that the  $\text{I}^-$  is oxidized to a higher oxidation state ( $\text{I}_2$ ). Moreover, as shown in the digital photograph, the AC electrode immersed in the ethanol after the first charge process turned yellow, further indicating the existence of iodine in the oxidized state. During the discharge process, the peaks shifted to the lower energy state (619.03 and 630.3 eV), displaying the iodine in the reduced state.<sup>[60]</sup> The discharged AC electrode in the ethanol solution exhibited a clear solution, further validating the presence of iodine in the reduced state.

To illustrate the evolution of the surface chemistry during the consecutive electrochemical iodine storage period, XPS studies of the charged/discharged cathode after ten cycles are shown in Figure S3a. The peak position, peak shift, and peak intensity change of the I 3d after 10 charge/discharge cycle are similar to those of the 1st cycle. This implies that the electrolyte additive strongly favours the electrochemical oxidation and reduction of  $\text{I}^-$  ions and  $\text{I}_2$  elements in the repeated cycling operation. Moreover, the Mn 2p XPS results for the 10<sup>th</sup> charge/discharge cycle are also provided in Figure S3b, where the  $\text{Mn}^{2+}$  features are witnessed after the charging process could be, associated with the formation of  $\text{Mn}-\text{I}_2$ , detailed analysis needed to support this claim. A slight deviation was observed for the Mn 2p profile in the discharge process, the related mechanism needs further validation.

TEM studies of AC cathode at the charged/discharged after ten cycles are presented in Figure 4 to illustrate the structural evolution that occurred during the electrochemical iodine storage period. The ex situ TEM image shows triangular nanoparticles embedded in the carbon matrix of the AC cathode after the 10<sup>th</sup> charge. Electrochemical deposition of  $\text{I}_2$  may be responsible for the formation of these particles on the AC surface (Figure 4a). Elemental mapping confirms that the triangular nanoparticles are composed of I elements. This supports the claim of electrochemical  $\text{I}_2$  deposition (Figure 4i). After the 10<sup>th</sup> discharge, the ex-situ TEM image shows that triangular nanoparticles are no longer present in the carbon matrix of the AC cathode (Figure 4b). Furthermore, the elemental mapping analysis does not show any features related to element I (refer to Figure 4ii). Therefore, the in situ deposition/dissolution of  $\text{I}_2$  is reversibly accessible through the use of electrolyte additives during the electrochemical cycling process,

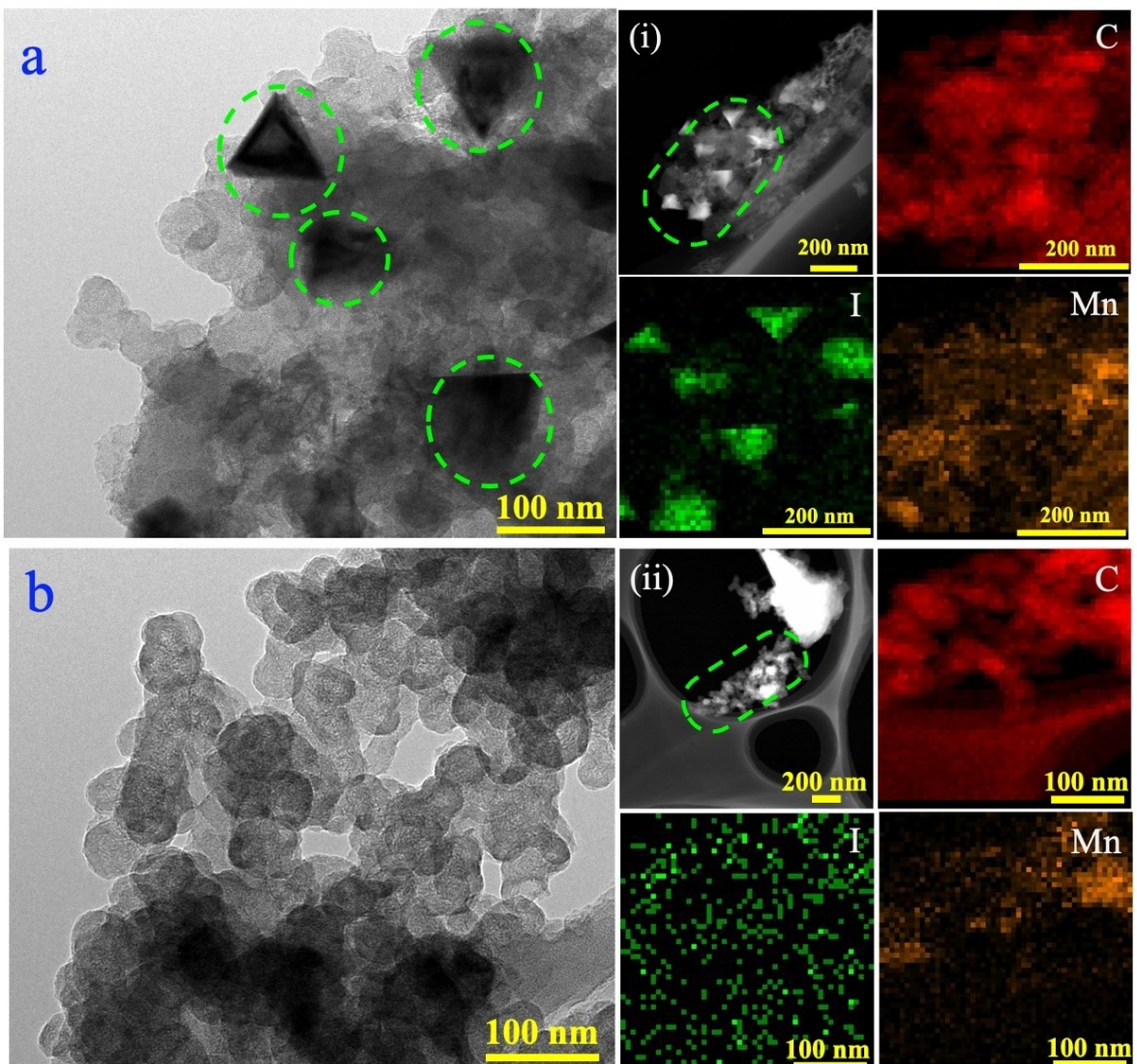


**Figure 4.** a) Ex situ TEM image of the AC cathode after a 10<sup>th</sup> cycle charging process, (i) Elemental mapping in brightfield image with corresponding elements of C, I, and Mn. b) Ex situ TEM image of the AC cathode after a 10<sup>th</sup> cycle discharge process, (ii) Elemental mapping in brightfield image with corresponding elements of C, I, and Mn.

as evidenced by the disappearance of the triangular nanoparticles during the discharge process.

The redox-active electrolyte additive induced stable electrochemical properties in the AC||AC coin cell configurations, offering a glimpse of the practical benefits and inspiring us to determine its prospects in the full-cell configurations further. Although Bi et al. reported the reversible electrodeposition of Mn metal powders in 1 M MnSO<sub>4</sub> and 1 M MnTFSI in DI water.<sup>[26]</sup> As previously reported by our group, the Mn metal powders for our AMIBs were only able to be electrodeposited in the first few cycles.<sup>[11]</sup> However, after a few cycles, the life of the cell ends due to plating failure. Our attempts at reversible plating using Mn powder for long cycles in the lab were unsuccessful after several trials. Hence, to demonstrate the energy-harvesting features of the iodine in the manganese electrolyte, we have constructed a hybrid-cell involving Zn–Mn alloy. The hybrid-cell

demonstration is only to showcase the iodine storage ability of the NaI in the presence of MC electrolyte. Thus given the previously recognized poor stability of Mn powder in aqueous electrolytes, an electrolytic Zn–Mn anode was favored as the anode in this study to construct AC||Zn–Mn hybrid full-cell.<sup>[11]</sup> The nature of the electrolytic Zn–Mn anode was confirmed using XRD, and the XRD pattern in Figure S4a depicts the existence of Zn–Mn features on the Cu foil.

The structural characteristics of the Zn–Mn coating were further examined with TEM analysis, where the Zn–Mn alloy featured a sheet-like morphology (Figure S4b and S4c). Furthermore, the elemental composition of the Zn–Mn alloy was distinguished using XPS, and it is presented in Figure S5. From Figure S5a, the deconvoluted Zn 2p spectrum at (1020.5 eV, Zn 2p<sub>3/2</sub>) and (1044 eV, Zn 2p<sub>1/2</sub>) indicates that the Zn element was present in the 0 state.<sup>[61,62]</sup> Notably, the existence of Mn<sup>0</sup>

features in the Zn–Mn alloy is also verified from the Mn 2p spectra in Figure S5b (641.1 eV, Mn 2p<sub>3/2</sub> and 653.4 eV, Mn 2p<sub>1/2</sub>).<sup>[63]</sup> The relative intensity of the Zn 2p peaks was higher than that of the Mn 2p (Figure S5c), indicating that the Zn had a major share in the Zn–Mn alloy. Moreover, the inductively coupled plasma optical electron microscopy (ICP-OES) analysis indicated that 0.13 wt% of the Mn existed in the Zn–Mn alloy (Table S1). Electrochemical Zn deposition features in the NMC electrolyte were established in unsymmetrical Cu|Zn–Mn cells at 1 mVs<sup>-1</sup> from −0.2 to 0.5 V. The CV curves proved the reversibility of the Zn plating/stripping process (Figure S6a). Similarly, the plating/stripping features were estimated in symmetrical Zn–Mn||Zn–Mn cells at 0.5 mA cm<sup>-2</sup> with a charge/discharge time of 1 h (Figure 5a). The electrochemical plating/stripping process for the Zn–Mn alloy system employed in this study is more complicated because the electrolyte carrying MC contains Mn<sup>2+</sup> ions and no Zn<sup>2+</sup> ions.<sup>[64]</sup> Generally, Zn has a higher redox potential (−0.76 V vs. SHE) than Mn (−1.19 V vs. SHE), so Zn could be reduced before Mn is reduced. Therefore, the involvement of Zn could be the predominant process on the anode side. During the plating stage, a single pulse is observed (Figure S6a). However, during the stripping stage, a peak splitting is noticed. This could be due to the dissociation of Mn<sup>2+</sup> along with the Zn<sup>2+</sup> ions. This complexity is reflected in the time vs voltage response as well.

In specific, the overpotentials of the plating/stripping voltage profiles were higher in the initial cycling (1–10 h, highlighted in the insert), stabilized after 40 h of cycling, and then retained a stable voltage profile close to the cycling (90–100 h, highlighted in the insert). The difference in voltage profiles observed during the plating and stripping cycles is linked to the intricate process of Zn plating in the absence of Zn<sup>2+</sup> ions in the electrolyte. Therefore, it is expected that using a definite Mn-rich anode will enhance the overall plating and stripping life. Ex-situ SEM studies were conducted on the Zn–Mn anode after 10 cycles in the Zn–Mn||Zn–Mn configuration at 0.5 mA cm<sup>-2</sup> to investigate the plating behaviour of the Zn–Mn anode. The results, presented in Figure S6b and S6c, reveal that the surface of the Zn–Mn anode has a scattered flake-like morphology, indicating compact and stable Zn plating even in the absence of Zn electrolyte. This observation confirms that the cycle life of the AC||Zn–Mn hybrid full-cell could be maintained when the plating efficacy and reversibility of the Zn–Mn alloy are maintained.

Subsequently, the AC||Zn–Mn hybrid full-cell configuration was constructed, and its electrochemical properties were investigated. Figure 5b demonstrates the commendable rate performance of the full-cell system, and reversible capacities of 160, 163.5, 165.3, 164.1, 152.6, and 142.4 mAh g<sup>-1</sup> were logged at 0.15, 0.3, 0.5, 1.0, 1.5, and 2.0 A g<sup>-1</sup>, respectively. Specifically,

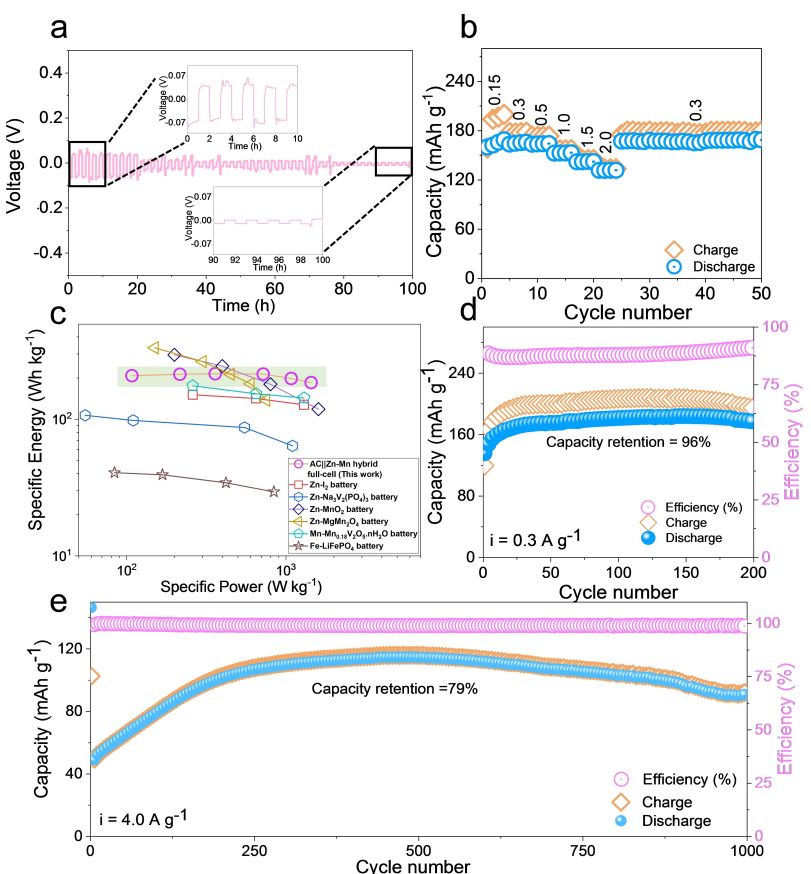


**Figure 5.** a) Time-Voltage curve of Zn–Mn||Zn–Mn anode in the NMC electrolyte at 0.5 mA/cm<sup>2</sup>, b) Rate performance output of the AC||Zn–Mn hybrid full-cell at various current rates, c) Ragone plot comparing the specific energy and power output of the AC||Zn–Mn hybrid full-cell with other state-of-the-art battery systems, Cycle-life profile of AC||Zn–Mn hybrid full-cell at d) 0.3 A g<sup>-1</sup>, and e) 4.0 A g<sup>-1</sup>.

the reversible capacity quickly recovered to 167.2 mAh g<sup>-1</sup> when the current rate was reduced to 0.3 A g<sup>-1</sup>, indicating highly reversible electrochemical I<sub>2</sub>/2I<sup>-</sup> redox features. The resulting voltage outputs exhibited identical voltage profiles with a stable working voltage of 1.3 V, indicating minimal voltage polarization in the AC||Zn–Mn hybrid full-cell configuration (Figure S7a). The Ragone plot (calculated based on the mass of the cathode only) in Figure 5c compares the energy and power features of the present AC||Zn–Mn hybrid full-cells with the existing standard aqueous metal batteries. It is worth noting that the energy output of the AC||Zn–Mn hybrid full-cell system stands out at 185 Wh kg<sup>-1</sup> at a high power of 2600 W kg<sup>-1</sup>, which is equivalent to the typical aqueous metal batteries compared here, including Zn–I<sub>2</sub>,<sup>[60]</sup> Zn–Na<sub>3</sub>V<sub>2</sub>(PO<sub>4</sub>)<sub>3</sub>,<sup>[65]</sup> Zn–MnO<sub>2</sub>,<sup>[66]</sup> Zn–MgMn<sub>2</sub>O<sub>4</sub>,<sup>[8]</sup> Mn–Mn<sub>0.18</sub>V<sub>2</sub>O<sub>5</sub>.nH<sub>2</sub>O,<sup>[26]</sup> and Fe–LiFePO<sub>4</sub>.<sup>[67]</sup> Next, the lifecycle of the full-cell configuration was tested at 0.3 A g<sup>-1</sup>, and the cycle life profile is provided in Figure 5d. The AC||Zn–Mn hybrid full-cell completed 200 cycles while maintaining a capacity of 177.2 mAh g<sup>-1</sup> with 96% capacity retention to the maximum capacity output (184 mAh g<sup>-1</sup>, 144<sup>th</sup> cycle). The corresponding voltage vs. capacity profile can be found in Figure S7b. Moreover, long-term electrochemical 2I<sup>-</sup>/I<sub>2</sub> redox features of the AC||Zn–Mn hybrid full-cell configuration were monitored at a high current density of 4.0 A g<sup>-1</sup> for 1000 cycles (Figure 5e). The cycle life output exhibited semi-parabolic behavior characterized by low capacity (40 mAh g<sup>-1</sup>) in the first cycle, the activation capacity (114.7 mAh g<sup>-1</sup>) at the 486<sup>th</sup> cycle, and finally the reversible capacity of 91 mAh g<sup>-1</sup> after the 1,000<sup>th</sup> cycle.

The tested AMIBs exhibited stable electrochemical performance and durability in both half-cell and hybrid configurations, and we matched the capabilities with the established battery system that operates on the Mn<sup>2+</sup> ion storage properties (Table S2). Although the comparison is complex due to varying modes of the electrochemical charge storage mechanism, different electrolytes, and test voltage ranges used in the respective reports, the present comparison can promote a better appreciation of the importance of the I<sub>2</sub>/I<sup>-</sup> conversion chemistry identified in this study. The AMIBs adopting the I<sub>2</sub>/I<sup>-</sup> conversion chemistry achieved advanced cycle stability and capacity retention characteristics over MIBs based on the Mn<sup>2+</sup> intercalation and enolisation redox chemistry. The comparison clearly highlights that the AC cathode with I<sub>2</sub>/I<sup>-</sup> conversion chemistry has a substantial advantage over the other cathode types with an intercalation mechanism.

The working mechanism of the AC||Zn–Mn hybrid full-cell in the NMC electrolyte is schematically illustrated in Figure S8 based on the combined electrochemical results and the ex-situ XPS results of the AC||AC and AC||Zn–Mn hybrid full-cell in the NMC electrolytes. Initially, the electrolyte additive, i.e., NaI, is dissociated into 2Na<sup>+</sup> and 2I<sup>-</sup> ions. Since Zn<sup>2+</sup> is reduced before the deposition of Mn when Mn–Zn alloy is used as the anode.<sup>[64]</sup> We have considered the participation of Zn<sup>2+</sup> as a primary anode reaction to express the working mechanism of the AC||Zn–Mn hybrid full cell. We are expecting feature efforts of direct use of the Mn-based alloy could bring out the

Mn-plating supported full-cell, which we are currently working on.



The 2I<sup>-</sup> ions are oxidized during the charging process and converted into I<sub>2</sub> species. The electron compensation is balanced by the Zn $\rightarrow$ Zn<sup>2+</sup> + 2e<sup>-</sup> reaction, the whole process being electrochemically reversible and providing the capacity and voltage output. These results demonstrate that the AC||AC coin cell output can be successfully extended to prototype AC||Zn–Mn hybrid full-cells, yet certain challenges need to be addressed before considering AC||Zn–Mn hybrid full-cells for practical applications. In specific, the cycling stability is significantly higher in the half-cell system compared to the hybrid full-cell, which exhibits fading behaviour over time. The half-cell system does not face the same challenges with dendrite growth and battery failure as the hybrid full-cell, where repeated cycling leads to anode deterioration and internal short circuits caused by metal needles on the anode side. To extend the life of the anode, dendrite growth can be reduced through the use of protective coatings, tailored electrolyte structures, and electrolyte additives.<sup>[32,68]</sup> Implementing the above strategies could enhance the cycle-life of a full-cell system if a definite Mn metal is used as an anode. The direct utilization of Mn-based anode material is essential to maximizing the cost savings and sustainability of the AMIBs. However, the use of Mn metal itself poses a challenge. The formulation of alloy-type anodes and their impact on the cycle life of AMIBs still requires further investigation. Moreover, the effects of redox-active electrolytes on the anode/cathode side during the cycling process need to be elucidated using operando studies. Finally, the optimization of the amount of the redox-active additive introduced to the electrolyte and the determination of its impacts on the capacity and cycling stability output need special attention.

### 3. Conclusions

In summary, this study developed AMIBs utilizing commercial AC and NMC redox-active electrolytes. The reversible iodine redox reaction was established using *ex-situ* XPS. Examination of joint electrochemical outputs and *ex-situ* outputs revealed that the reversible iodine conversion reaction (2I<sup>-</sup>/I<sub>2</sub>) holds the capacity output of MIBs. These AMIBs achieved a high discharge capacity of ~180.5 mAh g<sup>-1</sup> at 0.1 A g<sup>-1</sup>, a high-rate output (121 mAh g<sup>-1</sup> at 2.0 A g<sup>-1</sup>), and extremely stable long cycles (10,000 cycles with 91% capacity retention at 2.0 A g<sup>-1</sup>). Furthermore, this study demonstrated the potential of the AC||Zn–Mn hybrid full-cell configuration utilizing a hybrid anode (Zn–Mn) and revealed an admirable electrochemical property. Still, it is vital to choose appropriate Mn-based anode materials to achieve the true potential of AMIBs.

## Experimental Section

### Preparation of Electrodes

For the positive electrode, commercial AC (AB520Y) purchased from MTI, Korea was used as is without any purification. For the anode side, Zn–Mn alloy was deposited on Cu foil (14 mm) using a chloride bath containing 0.4 M  $\text{ZnCl}_2$ , 1.4 M  $\text{MnCl}_2 \cdot \text{H}_2\text{O}$ , 2.3 KCl, and 0.4 M  $\text{H}_3\text{BO}_3$ .<sup>[69]</sup> Then Galvanostatic plating was performed at a current density of 1 mA/cm<sup>2</sup> for 30 min with the zinc anode. After the plating, the Cu foil was retrieved, cleaned with deionized (DI) water, and dried at 80°C for 12 h in a vacuum furnace.

### Materials and Characterization

A Shimadzu X-ray diffractometer ( $\text{CuK}\alpha$  radiation ( $\lambda = 1.54056 \text{ \AA}$ )) operating at 40 kV and 30 mA within a scanning range ( $2\theta$ ) of 10–60° in 0.01° steps was used to validate the crystalline nature of the electrodes from the X-ray diffraction (XRD) patterns. Field-emission scanning electron microscopy (FE-SEM, S-4700 Hitachi) and Field-emission transmission electron microscopy (FE-TEM, Philips Tecnai F20 at 200 keV, KBSI, Chonnam National University, South Korea) were also used. A Micrometric ASAP 20220 (Norcross, GA, USA) was used to perform nitrogen adsorption and desorption measurements. The Brunauer–Emmett–Teller (BET) method was used to evaluate the surface area of the electrodes. An X-ray photoelectron spectrometer (XPS, Thermo VG Scientific instruments, Multilab 2000) equipped with Al  $\text{K}\alpha$  as the X-ray source was used to examine the redox features of the electrodes before and after the electrochemical process (the spectrometer was calibrated with a C 1s peak (binding energy 284.6 eV)).

### Electrochemical Measurements

The working electrode was prepared by mixing 80 wt.% of AC, 10 wt.% of super P, and 10 wt.% of polyvinylidene fluoride in the presence of N-methyl-2-pyrrolidone into a slurry and pasted onto a stainless-steel foil by the doctor's blade method. It was then dried at 70°C under vacuum. Subsequently, the dried slurry was hot-pressed between a stainless-steel roller maintained at 120°C. The AC electrode was cut into circular discs and used as both a cathode (14 mm, mass loading range of 2.8–4.0 mg) and anode (16 mm, mass loading range of 6.0–8.0 mg) (the mass ratio changes with the coating thickness). 2032-type coin cells were constructed in an open-air atmosphere by packing glass fiber with electrolytes between the two electrodes. The electrolyte was prepared by dissolving 1 M  $\text{Mn}(\text{ClO}_4)_2 + 0.1 \text{ M NaI}$  in DI water. Cyclic voltammetry (CV) were conducted with the Bio-Logic Science Instrument (VSP 1075). The galvanostatic charge/discharge analysis results were recorded at room temperature using TOYO and TOSCAT between 1.1 and –1.2 V. The hybrid full-cell configuration of the AMIBs was assembled using the Zn–Mn alloy as an anode in a CR 2032-type cell.

### Specific Power and Specific Energy Calculation

The determination of specific energy can be achieved by considering the capacity and voltage output of the cathode.<sup>[70]</sup>

Specific energy  $E$  (Wh kg<sup>-1</sup>) = Specific capacity × voltage (average working voltage)

The applied current density and cathode voltage output can be used to calculate specific power.

Specific power  $P$  (W kg<sup>-1</sup>) =  $I \times V/2 m$ , Where  $I$  is the applied current (A),  $V$  is the average working voltage (V), and  $m$  is the active mass on the cathode side.

### Acknowledgements

This work was supported by the National Research Foundation of Korea (NRF) grant funded by the Korea government (MSIT) (NRF-2018R1A5A1025224). This research is also funded by Hanoi University of Science and Technology (HUST) under project number T2022-XS-001.

### Conflict of Interests

There are no conflicts to declare.

### Data Availability Statement

The data that support the findings of this study are available from the corresponding author upon reasonable request.

- [1] K. Lu, H. Zhang, B. Song, W. Pan, H. Ma, J. Zhang, *Electrochim. Acta* **2019**, 296, 755.
- [2] Y. Liang, Y. Yao, *Nat. Rev. Mater.* **2023**, 8, 109.
- [3] G. Yasin, M. Arif, J. Ma, S. Ibraheem, D. Yu, L. Zhang, D. Liu, L. Dai, *Inorg. Chem. Front.* **2022**, 9, 1058.
- [4] G. Yasin, M. Arif, T. Mehtab, X. Lu, D. Yu, N. Muhammad, M. T. Nazir, H. Song, *Energy Storage Mater.* **2020**, 25, 644.
- [5] G. Yasin, S. Ali, S. Ibraheem, A. Kumar, M. Tabish, M. A. Mushtaq, S. Ajmal, M. Arif, M. A. Khan, A. Saad, L. Qiao, W. Zhao, *ACS Catal.* **2023**, 13, 2313.
- [6] L. Chen, Q. Gu, X. Zhou, S. Lee, Y. Xia, Z. Liu, *Sci. Rep.* **2013**, 3, 1946.
- [7] Q. Zhang, Y. Ma, Y. Lu, L. Li, F. Wan, K. Zhang, J. Chen, *Nat. Commun.* **2020**, 11, 4463.
- [8] V. Soundharajan, B. Sambandam, S. Kim, V. Mathew, J. Jo, S. Kim, J. Lee, S. Islam, K. Kim, Y.-K. Sun, J. Kim, *ACS Energy Lett.* **2018**, 3, 1998.
- [9] M. Han, J. Zhou, H. J. Fan, *Trends Chem.* **2023**, 5, 214.
- [10] S. Zhu, Q. Wang, J. Ni, *EnergyChem* **2023**, 5, 100097.
- [11] V. Soundharajan, S. Nithiananth, J. Lee, K. Sakthiabirami, D. T. Pham, J. H. Kim, J.-Y. Hwang, J. Kim, *J. Power Sources* **2023**, 558, 232542.
- [12] V. Soundharajan, S. Nithiananth, J. Lee, J. H. Kim, J.-Y. Hwang, J. Kim, *J. Mater. Chem. A* **2022**, 10, 18162.
- [13] G. Zampardi, F. La Mantia, *Nat. Commun.* **2022**, 13, 687.
- [14] D. Lin, Y. Li, *Adv. Mater.* **2022**, 34, 2108856.
- [15] Z. Zhang, F. Mo, W. Ling, M. Cui, J. Wei, M. Yu, Y. Huang, *Energy Fuels* **2022**, 36, 5979.
- [16] S. Gheytani, Y. Liang, F. Wu, Y. Jing, H. Dong, K. K. Rao, X. Chi, F. Fang, Y. Yao, *Adv. Sci.* **2017**, 4, 1700465.
- [17] Q. Liu, F. Ye, K. Guan, Y. Yang, H. Dong, Y. Wu, Z. Tang, L. Hu, *Adv. Energy Mater.* **2023**, 13, 2202908.
- [18] D. Lin, D. Rao, S. Chiavoloni, S. Wang, J. Q. Lu, Y. Li, *Nano Lett.* **2021**, 21, 4129.
- [19] Y. Li, L. Liu, H. Li, F. Cheng, J. Chen, *Chem. Commun.* **2018**, 54, 6792.
- [20] Q. Chen, S. Chen, J. Zhang, *J. Power Sources* **2023**, 556, 232529.
- [21] C. Choi, D. S. Ashby, D. M. Butts, R. H. DeBlock, Q. Wei, J. Lau, B. Dunn, *Nat. Rev. Mater.* **2020**, 5, 5.
- [22] H. Shao, Y.-C. Wu, Z. Lin, P.-L. Taberna, P. Simon, *Chem. Soc. Rev.* **2020**, 49, 3005.
- [23] W. Wu, C. Li, Z. Wang, H.-Y. Shi, Y. Song, X.-X. Liu, X. Sun, *Chem. Eng. J.* **2022**, 428, 131283.
- [24] S. Yang, C. Li, H. Lv, X. Guo, Y. Wang, C. Han, C. Zhi, H. Li, *Small Methods* **2021**, 5, 2100611.
- [25] C. Bai, H. Jin, Z. Gong, X. Liu, Z. Yuan, *Energy Storage Mater.* **2020**, 28, 247.

- [26] S. Bi, S. Wang, F. Yue, Z. Tie, Z. Niu, *Nat. Commun.* **2021**, *12*, 6991.
- [27] W. Fan, X. Xiong, Y. Xu, L. Fu, T. Wang, Y. Ma, R. Holze, Y. Wu, *Next Energy* **2023**, *1*, 100049.
- [28] S. W. D. Gourley, R. Brown, B. D. Adams, D. Higgins, *Joule* **2023**, *7*, 1415.
- [29] L. Miao, Z. Guo, L. Jiao, *Energy Materials* **2023**, *3*, 300014.
- [30] L. Meng, X. Ji, M. Li, T. Liu, W. Dong, Y. Pan, L. Huang, S. Cheng, *Surfaces and Interfaces* **2022**, *29*, 101782.
- [31] S. Bi, H. Wang, Y. Zhang, M. Yang, Q. Li, J. Tian, Z. Niu, *Angew. Chem. Int. Ed.* **2023**, *62*, e202312982.
- [32] J. Ma, M. Wang, H. Zhang, L. Fu, W. Zhang, B. Song, S. Lu, Q. Chen, K. Lu, *Mater. Today* **2022**, *30*, 101146.
- [33] G. Lota, E. Frackowiak, *Electrochim. Commun.* **2009**, *11*, 87.
- [34] H. Yang, Y. Qiao, Z. Chang, H. Deng, P. He, H. Zhou, *Adv. Mater.* **2020**, *32*, 2004240.
- [35] Y. Zhang, T. Zhao, S. Yang, Y. Zhang, Y. Ma, Z. Wang, *J. Energy Chem.* **2022**, *75*, 310.
- [36] T.-T. Su, J.-B. Le, K. Wang, K.-N. Liu, C.-Y. Shao, W.-F. Ren, R.-C. Sun, *J. Power Sources* **2022**, *550*, 232136.
- [37] W. Shang, Q. Li, F. Jiang, B. Huang, J. Song, S. Yun, X. Liu, H. Kimura, J. Liu, L. Kang, *Nano-Micro Lett.* **2022**, *14*, 82.
- [38] Y. Yang, S. Liang, B. Lu, J. Zhou, *Energy Environ. Sci.* **2022**, *15*, 1192.
- [39] G. Chen, Y. Kang, H. Yang, M. Zhang, J. Yang, Z. Lv, Q. Wu, P. Lin, Y. Yang, J. Zhao, *Adv. Funct. Mater.* **2023**, *33*, 2300656.
- [40] Z. Sun, X. Han, D. Wang, *J. Energy Storage* **2023**, *62*, 106857.
- [41] Y. Ji, J. Xie, Z. Shen, Y. Liu, Z. Wen, L. Luo, G. Hong, *Adv. Funct. Mater.* **2023**, *33*, 2210043.
- [42] J. Zhang, Q. Dou, C. Yang, L. Zang, X. Yan, *J. Mater. Chem. A* **2023**, *11*, 3632.
- [43] L. Sun, K. Zhuo, Y. Chen, Q. Du, S. Zhang, J. Wang, *Adv. Funct. Mater.* **2022**, *32*, 2203611.
- [44] L.-C. Yu, Y.-C. Luo, W. Feng, S. Zhang, X. Zhang, *J. Mater. Chem. A* **2023**, *11*, 18911.
- [45] Q. Hu, S. Cui, K. Sun, X. Shi, W. Miao, X. Wang, H. Peng, G. Ma, *J. Energy Storage* **2023**, *68*, 107815.
- [46] X. Cai, Y. Xiao, W. Sun, F. Yang, *Electrochim. Acta* **2022**, *406*, 139861.
- [47] R. Thangavel, K. Kaliyappan, K. Kang, X. Sun, Y.-S. Lee, *Adv. Energy Mater.* **2016**, *6*, 1502199.
- [48] J. J. Hong, L. Zhu, C. Chen, L. Tang, H. Jiang, B. Jin, T. C. Gallagher, Q. Guo, C. Fang, X. Ji, *Angew. Chem. Int. Ed.* **2019**, *58*, 15910.
- [49] J. Pu, L. Wang, J. Huang, Q. Chen, Y. Jin, J. Chen, *Diamond Relat. Mater.* **2023**, *132*, 109684.
- [50] H. Chen, F. Yu, G. Wang, L. Chen, B. Dai, S. Peng, *ACS Omega* **2018**, *3*, 4724.
- [51] T. Liu, X. Li, C. Xu, H. Zhang, *ACS Appl. Mater. Interfaces* **2017**, *9*, 4626.
- [52] Y. Zhang, C. Wei, M.-X. Wu, Y. Wang, H. Jiang, G. Zhou, X. Tang, X. Liu, *Chem. Eng. J.* **2023**, *451*, 138915.
- [53] Y. Yang, S. Guo, Y. Pan, B. Lu, S. Liang, J. Zhou, *Energy Environ. Sci.* **2023**, *16*, 2358.
- [54] Y. Lyu, J. A. Yuwono, P. Wang, Y. Wang, F. Yang, S. Liu, S. Zhang, B. Wang, K. Davey, J. Mao, Z. Guo, *Angew. Chem. Int. Ed.* **2023**, *62*, e202303011.
- [55] S. Niu, B. Zhao, D. Liu, *ACS Appl. Mater. Interfaces* **2023**, *15*, 25558.
- [56] S. Kim, V. Soundharajan, S. Kim, B. Sambandam, V. Mathew, J.-Y. Hwang, J. Kim, *Nanomaterials* **2021**, *11*, 1905.
- [57] D. Yu, A. Kumar, T. A. Nguyen, M. T. Nazir, G. Yasin, *ACS Sustainable Chem. Eng.* **2020**, *8*, 13769.
- [58] V. Soundharajan, B. Sambandam, M. H. Alfaruqi, S. Kim, J. Jo, S. Kim, V. Mathew, Y. Sun, J. Kim, *J. Mater. Chem. A* **2020**, *8*, 770.
- [59] L. Yan, T. Liu, X. Zeng, L. Sun, X. Meng, M. Ling, M. Fan, T. Ma, *Carbon* **2022**, *187*, 145.
- [60] Q. Guo, H. Wang, X. Sun, Y. Yang, N. Chen, L. Qu, *ACS Materials Lett.* **2022**, *4*, 1872.
- [61] V. Soundharajan, B. Sambandam, S. Kim, M. H. Alfaruqi, D. Y. Putro, J. Jo, S. Kim, V. Mathew, Y.-K. Sun, J. Kim, *Nano Lett.* **2018**, *18*, 2402.
- [62] L. Wang, K.-W. Huang, J. Chen, J. Zheng, *Sci. Adv.* **2023**, *5*, eaax4279.
- [63] V. Soundharajan, J. Lee, S. Kim, J. H. Kim, J.-Y. Hwang, J. Kim, *Batteries & Supercaps* **2023**, *6*, e202200527.
- [64] V. Soundharajan, S. Nithiananth, G. Alfaza, J. Piao, D. P. Tung, E. H. Ang, J. Kasnatscheew, M. Winter, J. H. Kim, J. Kim, *J. Mater. Chem. A* **2024**, *12*, 11403.
- [65] G. Li, Z. Yang, Y. Jiang, C. Jin, W. Huang, X. Ding, Y. Huang, *Nano Energy* **2016**, *25*, 211.
- [66] M. H. Alfaruqi, J. Gim, S. Kim, J. Song, J. Jo, S. Kim, V. Mathew, J. Kim, *J. Power Sources* **2015**, *288*, 320.
- [67] X. Wu, A. Markir, Y. Xu, C. Zhang, D. P. Leonard, W. Shin, X. Ji, *Adv. Funct. Mater.* **2019**, *29*, 1900911.
- [68] W. Shang, J. Zhu, Y. Liu, L. Kang, S. Liu, B. Huang, J. Song, X. Li, F. Jiang, W. Du, Y. Gao, H. Luo, *ACS Appl. Mater. Interfaces* **2021**, *13*, 24756.
- [69] Y. Deo, R. Ghosh, A. Nag, D. V. Kumar, R. Mondal, A. Banerjee, *Electrochim. Acta* **2021**, *399*, 139379.
- [70] V. Soundharajan, M. H. Alfaruqi, G. Alfaza, J. Lee, S. Lee, S. Park, S. Nithiananth, D. T. Pham, J.-Y. Hwang, J. Kim, *J. Mater. Chem. A* **2023**, *11*, 15518.

Manuscript received: February 29, 2024  
Revised manuscript received: April 8, 2024  
Accepted manuscript online: April 28, 2024  
Version of record online: June 3, 2024